B-Site Doping Engineering of Zero-Dimensional Perovskite Cs_3MnCl_5: Stability Improvement and Multicolor Luminescence Regulation

Y.F. Zhang*, Y. Li and S.Y. Shen

College of Mathematics and Physics, Shanghai University of Electric Power, 1851 Hucheng Ring Road, New Pudong District, 201306 Shanghai, People's Republic of China

Received: 09.03.2026 & Accepted: 25.05.2026

Doi: 10.12693/APhysPolA.149.145 *e-mail: 2009000018@shiep.edu.cn

Mn-based zero-dimensional metal halide perovskites have attracted much attention in the field of lead-free optical materials due to their rich manganese reserves, environmental friendliness, and the unique d–d transition characteristics of Mn^{2+}. However, the poor water and oxygen stability and single luminous color of the intrinsic material severely limit the practical applications. In this paper, high-quality all-inorganic zero-dimensional perovskite Cs_3MnCl_5 single crystals were successfully prepared by the vacuum solid-state reaction method, and the regulation mechanism of heterovalent ions (Ag^+, Ce^{3+}, Sb^{3+}) on the stability and luminescence properties of the materials was studied by B-site doping. X-ray diffraction and X-ray photoelectron spectroscopy analysis confirm that the doped ions successfully enter the Cs_3MnCl_5 lattice and occupy the Mn^{2+} sites, resulting in lattice expansion. Optical characterization shows that the intrinsic Cs_3MnCl_5 exhibits a bright green emission at 520 nm derived from the $^4T_1$–$^6A_1$ transition of the Mn^{2+} tetrahedral coordination. Ag^+ doping significantly improves the environmental stability of the material, and the maintenance time of green fluorescence in a high-humidity environment increases by more than ten times compared with the intrinsic material. Ce^{3+} doping induces the dual luminescence of violet ($\sim$ 420 nm) derived from the Ce^{3+} $5d$–$4f$ transition and green emission from Mn^{2+}, and the dual intensity ratio can be flexibly adjusted by excitation wavelength to achieve cold white light emission at 365 nm excitation. Sb^{3+} doping introduces orange emission ($\sim$ 585 nm), derived from the Sb^{3+} $^3P_1$–$^1S_0$ transition, resulting in yellow–green fluorescence. This work provides a new design idea for the application of Mn-based zero-dimensional halides.

topics: metal halide perovskites, Cs_3MnCl_5, luminescence, doping

1. Introduction

Metal halide perovskites ABX_3 (A = Na^+, K^+, Cs^+, Rb^+, etc.; B = Pb^{2+}, Sn^{2+}, etc.; X = Cl^-, Br^-, I^-) exhibit unique properties useful in photovoltaic devices, light-emitting diodes (LEDs), laser systems, and scintillator materials [1–3]. Their advantages lie in the tunable bandgap and ease of preparation, which makes metal halide perovskites a novel and efficient material for photoelectric conversion [4, 5]. Compared to three-dimensional (3D) halide perovskites with a continuous octahedral framework, zero-dimensional (0D) metal halide perovskites consist of isolated and separated luminescent centers, offering significant advantages in luminescent performance [6–8]. Thanks to the strong quantum confinement effect and efficient exciton localization effect, zero-dimensional perovskites exhibit large exciton binding energy, which can greatly suppress non-radiative recombination processes, thereby achieving high photoluminescence quantum yield (PLQY) close to 100% [9–11]. Meanwhile, their structural feature in the form of separated luminescent centers effectively blocks ion migration and phase decomposition pathways, making these systems far superior to 3D perovskites in terms of environmental and thermal stability, as well as photostability [9, 12]. In addition, the highly localized electronic structure facilitates the generation of self-trapped excitons, enabling wide-spectrum emission with a large Stokes shift, thus allowing the material to exhibit tunable luminescence across the ultraviolet to near-infrared wavelength range [13, 14]. These advantages make 0D metal halide perovskites ideal candidates for high-performance light-emitting devices.

In recent years, all-inorganic zero-dimensional metal halide perovskites have quickly become a research hotspot in the field of optoelectronic materials due to their unique crystal structure, which is characterized by advantages such as large exciton

binding energy, high luminescence efficiency, and solution processing [15–17]. Due to the strong spin–orbit coupling, the radiation recombination rate of lead-based zero-dimensional Cs_4PbX_6 is fast, but the thermal quenching effect causes its PLQY to be less than 0.1%, and the inherent toxicity of Pb also seriously limits the practical application of this system [18, 19]. In the Cs_4GeX_6 system, although a large Stokes shift and strong exciton–phonon coupling are observed, the luminescence is severely quenched at room temperature due to excessive structural relaxation, rendering the material almost non-luminescent [18]. In tin-based zero-dimensional metal halide perovskite materials, such as Cs_4SnX_6, efficient photoluminescence with a PLQY close to 100% can be achieved by enhancing the rigidity of the octahedra. However, Sn^{2+} is prone to oxidation, resulting in poor stability of the intrinsic material [20, 21]. Meanwhile, copper-based zero-dimensional metal halide perovskites, such as $Cs_3Cu_2I_5$ and $CsCu_2I_3$, exhibit efficient blue or yellow light emission originating from self-trapped exciton emission. The PLQY of $Cs_3Cu_2I_5$ single crystals can reach up to 90%, but their emission color tunability is limited [22]. Compared to these materials, Mn-based all-inorganic zero-dimensional metal halide perovskites have garnered significant attention in recent years as an ideal system for lead-free luminescent materials, owing to the abundant reserves of manganese, environmental friendliness, and the unique *d–d* transition characteristics of Mn^{2+} [23–25]. By regulating the coordination environment of $[MnX_4]^{2-}$ tetrahedra or $[MnX_6]^{4-}$ octahedra, tunable luminescence from green to red can be achieved. Furthermore, modulation of the Mn–Mn distance can effectively tune the emission characteristics, making Mn-based metal halide perovskites highly attractive for applications in scintillators, light-emitting diodes, and sensing devices [26–28]. However, despite the significant advantages of such systems in lighting and anti-counterfeiting applications, the instability of the Mn^{2+} oxidation state, limited color tunability, and poor water–oxygen stability of Mn-based materials have restricted their practical implementation [29–31]. Element doping is an effective method to expand the emission spectrum of perovskites [32–36]. Owing to the isolated octahedral structure of 0D metal halide perovskite, where interactions between units are minimized, the properties of a single octahedron significantly determine the overall material characteristics. Partial substitution of elements within the polyhedral center can greatly alter the properties of 0D metal halides [32–35].

In this work, we focus on the preparation and regulation of the stability and optical properties of Cs_3MnCl_5 single crystals of all-inorganic zero-dimensional metal halide perovskite. High-quality Cs_3MnCl_5 single crystals were successfully prepared by the vacuum solid-state reaction method, and X-ray diffraction (XRD) analysis confirmed their high phase purity and good crystallinity. Photoluminescence tests reveal that the material exhibits a broad-spectrum green emission at 520 nm, originating from the $^4T_1$–$^6A_1$ transition of tetrahedrally coordinated Mn^{2+}. Furthermore, the solid-state reaction method demonstrates significant advantages over traditional liquid-phase methods in terms of synthesis convenience and sample purity. Given the ubiquitous moisture and stability issues in Mn-based systems, we systematically investigated the regulation mechanism of the material stability and luminescence properties through B-site doping engineering by introducing heterovalent ions. The study found that Ag^+ doping can effectively inhibit the hydration transformation of Cs_3MnCl_5 in high-humidity environments, significantly extending the stability. The successful doping of Ce^{3+} and Sb^{3+} allows for tuning of the luminescent color of Cs_3MnCl_5. Ce^{3+} doping induces dual-peak emission in purple and green, and the intensity ratio of the dual peaks can be flexibly adjusted by excitation wavelength, providing a feasible approach to achieving single-matrix white light emission. This study not only demonstrates an efficient solid-state synthesis method for preparing Cs_3MnCl_5 luminescent single crystals but also presents a method for enhancing the stability of the material and tuning its optical properties through doping, achieving multicolor luminescence. It provides new design ideas for the exploration of Mn-based zero-dimensional halide perovskite materials in white light-emitting diodes and multicolor anti-counterfeiting applications.

2. Experimental methods

2.1. Chemicals

All materials were used directly without further purification. They are as follows: CsCl (Aladdin, 99.9%), $MnCl_2$ (Aladdin, 99.99%), $SbCl_3$ (Aladdin, 99.8%), AgCl (Aladdin, 99.9%), $CeCl_3$ (Aladdin, 99.8%).

2.2. Preparation of single crystals

The preparation of metal halide perovskite Cs_3MnCl_5 single crystals was performed by the vacuum solid-phase method. In the glove box with argon gas circulation purification, the moisture and oxygen levels were kept below 0.01 ppm, and cesium chloride and manganese chloride were weighed using an electronic balance, carefully poured into an agate mortar, and mixed. Immediately after, the mixture was carefully ground for 1 h and loaded into a 9 mm quartz tube with a joint. Then the sealed joint was connected to the double-row pipe,

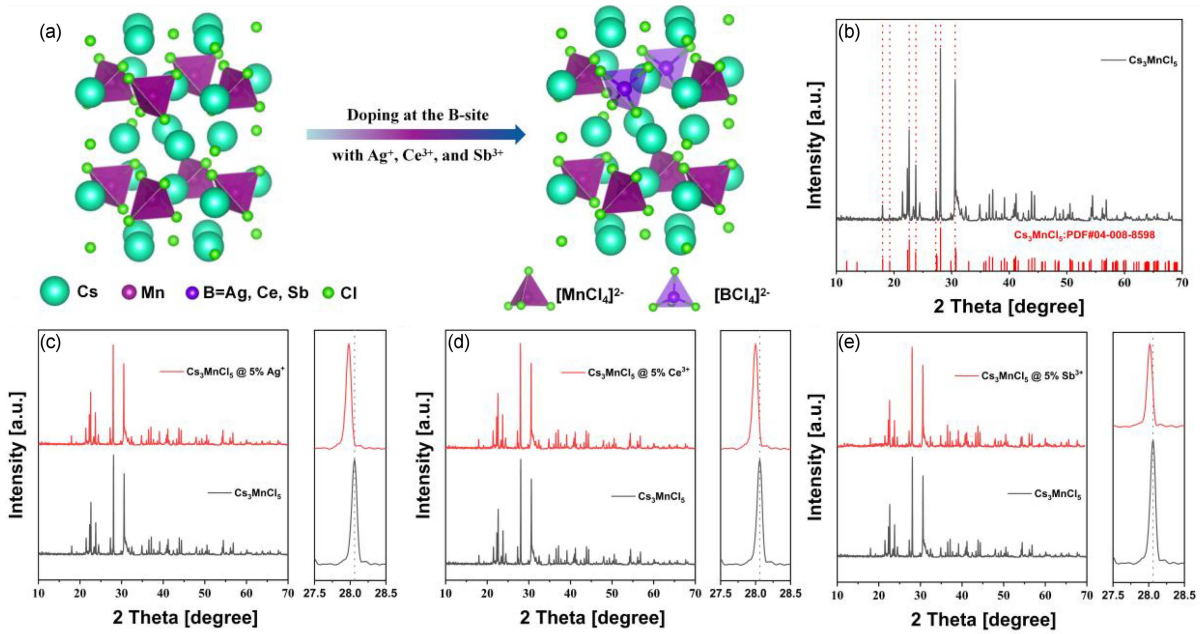

Fig. 1. Structural transition of B-doped Cs_3MnCl_5; (a) changes in the crystal structure; (b) XRD of Cs_3MnCl_5; (c) XRD of 5% Ag^+-doped Cs_3MnCl_5; (d) XRD of 5% Ce^{3+}-doped Cs_3MnCl_5; (e) XRD of 5% Sb^{3+}-doped Cs_3MnCl_5.

and the pumping was repeated 4 times in an atmosphere of argon gas. The first three times were to ensure the vacuum level in the quartz tube was 20–25 Pa, and the fourth time was to ensure the vacuum level in the quartz tube was 16–18 Pa, ensuring an oxygen-free and waterless atmosphere in the quartz tube. Subsequently, a hydrogen–oxygen flame was used for sealing. The sealed quartz capsules were placed in a muffle furnace at room temperature and heated to 800°C at a rate of 5°C/min. It was kept for 24 h and then cooled to room temperature at a rate of 0.2°C/min. Finally, Cs_3MnCl_5 single crystals were obtained. The preparation of B-doped Cs_3MnCl_5 was similar to the above method, with the addition of 5% silver chloride, 5% cerium chloride, and 5% antimony chloride.

2.3. Characterization

Powder X-ray diffraction (XRD) patterns were recorded on a Rigaku Ultima IV diffractometer using Cu K_α radiation ($\lambda = 1.5418$ Å). X-ray photoelectron spectroscopy (XPS) measurements were carried out by an ultra-high vacuum surface analysis system (Thermo Scientific ESCALAB 250Xi). Scanning electron microscopy (SEM) and corresponding energy-dispersive X-ray spectroscopy (EDS) measurements were performed using a Tescan MIRA3 field-emission scanning electron microscope. The steady-state photoluminescence (PL) was collected by a fluorescence spectrometer (Zolix OmniFluo-900).

3. Results and discussion

As shown in Fig. 1, the purpose of this paper is to regulate the stability and optical properties of Cs_3MnCl_5 by introducing heterovalent B elements (B = Ag^+, Ce^{3+}, Sb^{3+}) to replace Mn^{2+}. In recent years, most reported synthetic routes for Cs_3MnCl_5 single crystals rely on liquid-phase methods, which generally yield the target phase through indirect structural transformation rather than direct one-step crystallization. Xiao et al. [37] indirectly prepared a one-dimensional (1D) $CsMnCl_3(H_2O)$ single crystal with light emission by the liquid-phase method, and then, after contact with dimethylacetamide (DMAC) or dimethylformamide (DMF), its crystal structure can be changed from $CsMnCl_3(H_2O)$ to 0D Cs_3MnCl_5, emitting a faint green light. The loss of crystalline water is mainly induced by solvents, and 0D Cs_3MnCl_5 single crystals were obtained. Yang et al. [38] prepared Cs_3MnCl_5 single crystals by the hydrothermal method. When no doped ions were introduced, the crystal powder only emitted extremely faint green fluorescence. With the introduction of Zn^{2+}, the green fluorescence gradually intensified. When zinc : manganese = 4 : 1, the green fluorescence intensity was the highest. The analysis found that in the absence of zinc chloride, the sample was mainly composed of cesium chloride and a small amount of $Cs_2MnCl_4(H_2O)$, which indicates that Cs_3MnCl_5 cannot be directly formed by the aqueous synthesis method [38]. None of these methods can directly obtain Cs_3MnCl_5 single

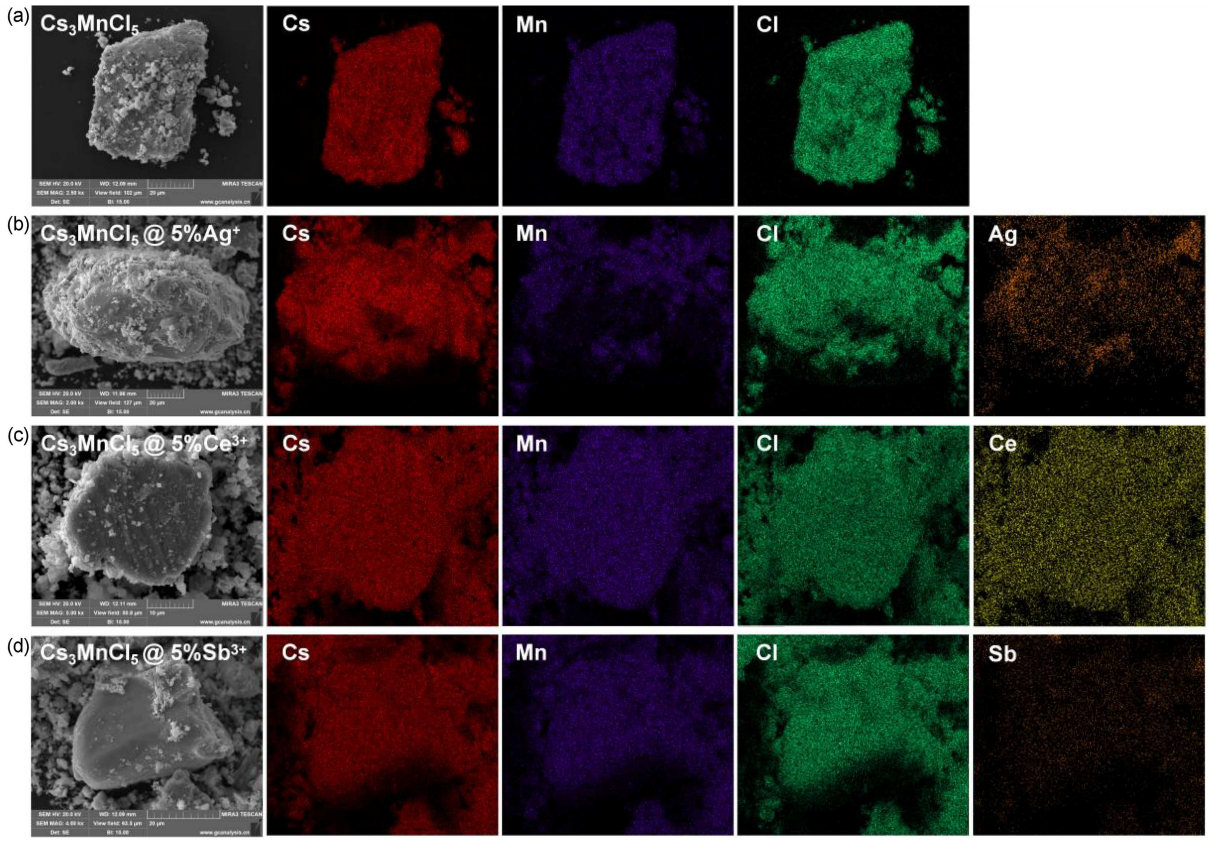

Fig. 2. SEM images and corresponding EDS elemental mappings of Cs_3MnCl_5 and doped samples; (a) pristine Cs_3MnCl_5; (b) 5% Ag^+-doped Cs_3MnCl_5; (c) 5% Ce^{3+}-doped Cs_3MnCl_5; (d) 5% Sb^{3+}-doped Cs_3MnCl_5.

crystals, and Cs_3MnCl_5 is indirectly synthesized by the liquid-phase method, which increases the cost and difficulty of preparation.

In this paper, Cs_3MnCl_5 single crystals were prepared by the solid-state reaction method. XRD test analysis found that the diffraction data of the sample was consistent with the standard spectrum PDF# (04-008-8598) of Cs_3MnCl_5, indicating that Cs_3MnCl_5 prepared in this study has a higher purity (Fig. 1b). All the main diffraction peaks of the sample (red dotted lines) are well aligned with the standard peaks, and a tiny residual peak of the raw material CsCl is observed at $2\theta = 21.5°$ in addition to the standard diffraction peaks of Cs_3MnCl_5, which is attributed to the loss during the weighing and grinding of the product, resulting in an uneven reaction [39]. Consistent with the above observations, the XRD pattern of the as-synthesized Cs_3MnCl_5 also matches well with that of the Sb^{3+}-doped Cs_3MnCl_5 system reported by Wang et al. [40], collectively confirming the successful synthesis of the target Cs_3MnCl_5 material. XRD patterns of the other doped samples are presented in Fig. 1c–e. All diffraction peaks of Ag^+-, Ce^{3+}-, and Sb^{3+}-doped Cs_3MnCl_5 shift systematically to lower 2θ angles relative to the pristine sample. The magnified views of the strongest (112) diffraction peak at 28.07° in the insets clearly demonstrate that the magnitude of the peak shift follows the order: Ag^+-doped > Ce^{3+}-doped > Sb^{3+}-doped Cs_3MnCl_5. This regular peak shift can be well explained by Bragg's law ($2d\sin(\theta) = n\lambda$). The ionic radii of Ag^+ (0.115 nm), Ce^{3+} (0.101 nm), and Sb^{3+} (0.076 nm) are all larger than that of the host Mn^{2+} (0.067 nm). The partial substitution of larger dopant cations for Mn^{2+} induces lattice expansion, which increases the interplanar spacing d. According to Bragg's law, an increase in d will result in a decrease in the diffraction angle θ, which is consistent with our experimental observations.

The morphology and elemental distribution of the as-prepared samples were characterized by SEM and EDS, as shown in Fig. 2. All samples exhibit irregular block-like crystal morphology with particle sizes ranging from 20 to 100 μm. The crystal surfaces are covered with a small amount of fine attached particles, consistent with the residual unreacted CsCl phase detected by XRD. The overall block-like crystal morphology is maintained after Ag^+, Ce^{3+}, or Sb^{3+} doping, indicating that the introduction of dopant ions does not fundamentally alter the crystal growth habit of Cs_3MnCl_5. The EDS elemental mapping images clearly demonstrate that Cs, Mn, Cl, and the corresponding dopant elements (Ag^+, Ce^{3+}, Sb^{3+}) are uniformly distributed throughout the entire crystal particles, without

TABLE I

The atomic composition of Cs_3MnCl_5 and B-doped Cs_3MnCl_5 (where B = Ag^+, Ce^{3+}, Sb^{3+}) determined by EDS.

Element	Line type	K Factor	Wt%	Wt% Sigma	Atomic %
Cs_3MnCl_5					
Cl	K series	0.07651	23.58	0.28	50.98
Mn	K series	0.02249	6.39	0.33	8.92
Cs	L series	0.21570	69.53	0.39	40.10
Total			100.00		100.00
Ag^+-doped Cs_3MnCl_5					
Cl	K series	0.08230	19.38	0.38	35.1
Mn	K series	0.01889	7.90	0.41	12.1
Cs	L series	0.24470	71.91	0.39	51.9
Ag	L series	0.00374	0.81	0.58	0.9
Total			100.00		100.00
Ce^{3+}-doped Cs_3MnCl_5					
Cl	K series	0.09862	15.38	0.30	35.8
Mn	K series	0.02848	13.25	0.29	19.9
Cs	L series	0.25411	71.03	0.51	44.1
Ce	L series	0.00173	0.34	0.55	0.2
Total			100.00		100.00
Sb^{3+}-doped Cs_3MnCl_5					
Cl	K series	0.08763	15.08	0.31	35.3
Mn	K series	0.02767	13.18	0.38	19.9
Cs	L series	0.25712	71.45	0.53	44.6
Sb	L series	0.00187	0.29	0.51	0.2
Total			100.00		100.00

obvious phase separation or dopant aggregation, providing direct evidence of the homogeneous doping of the guest ions into the Cs_3MnCl_5 host lattice.

Quantitative EDS results obtained at an acceleration voltage of 20 kV are summarized in Table I. Based on EDS results, the actual doping concentrations relative to Mn are approximately 7.4% for Ag^+, 1.0% for Ce^{3+}, and 1.0% for Sb^{3+}. When normalized to the Mn content, the measured atomic ratios of Cs : Mn : Cl are 4.49 : 1 : 5.72 for pristine Cs_3MnCl_5, 4.29 : 1 : 2.90 for Ag^+-doped Cs_3MnCl_5, 2.22 : 1 : 1.80 for Ce^{3+}-doped Cs_3MnCl_5, and 2.24 : 1 : 1.77 for Sb^{3+}-doped Cs_3MnCl_5, respectively. Although these values deviate from the ideal stoichiometric ratio of Cs_3MnCl_5 (3 : 1 : 5), the overall elemental composition confirms the formation of the target phase. All samples exhibit a consistent systematic deviation, i.e., generally higher Cs contents and significantly lower Cl contents. This systematic deviation can be mainly attributed to two factors:

(i) The inherent limitation of EDS technique under 20 kV — the Cl K_α line (2.6 keV) is a soft X-ray that is easily absorbed by the sample surface and the beryllium window of the instrument, leading to severe underestimation of the Cl content [41, 42], while the Cs L_α line (4.2 keV) has a much higher excitation efficiency, resulting in an overestimation of the Cs content;

(ii) The heterogeneous distribution of residual CsCl phase — as detected by XRD, a small amount of unreacted CsCl is unevenly distributed on the crystal surface. The measured atomic percentages of Ce and Sb are all lower than the nominal doping level of 5 at.%. For Ce^{3+}- and Sb^{3+}-doped samples, the large deviation is additionally caused by their contents being close to the detection limit of EDS, leading to large counting errors.

It should be noted that EDS is essentially a semi-quantitative surface analysis technique, and its core value lies in verifying the uniform distribution of elements rather than providing precise stoichiometric data. Combined with the systematic lattice expansion observed in XRD patterns and the uniform elemental distribution shown in EDS mappings, it can be conclusively demonstrated that the Ag^+, Ce^{3+},

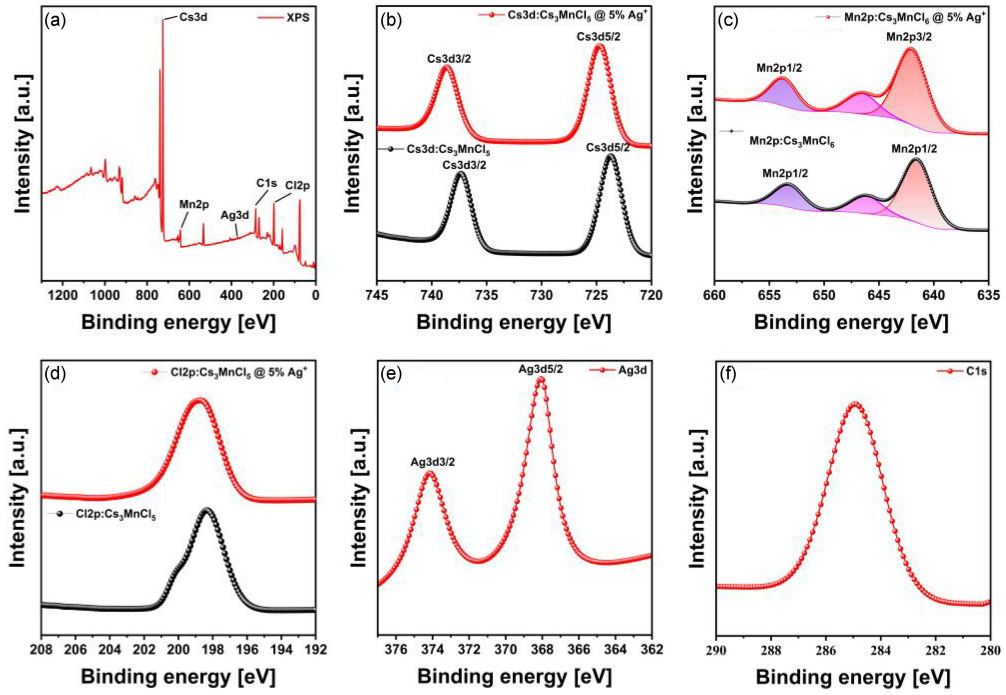

Fig. 3. XPS spectra of pristine Cs_3MnCl_5 (black lines) and 5% Ag^+-doped Cs_3MnCl_5 (red lines); (a) full survey spectrum; (b) high-resolution Cs 3*d* spectra; (c) high-resolution Mn 2*p* spectra; (d) high-resolution Cl 2*p* spectra; (e) high-resolution Ag 3*d* spectrum; (f) C 1*s* reference spectrum for binding energy calibration.

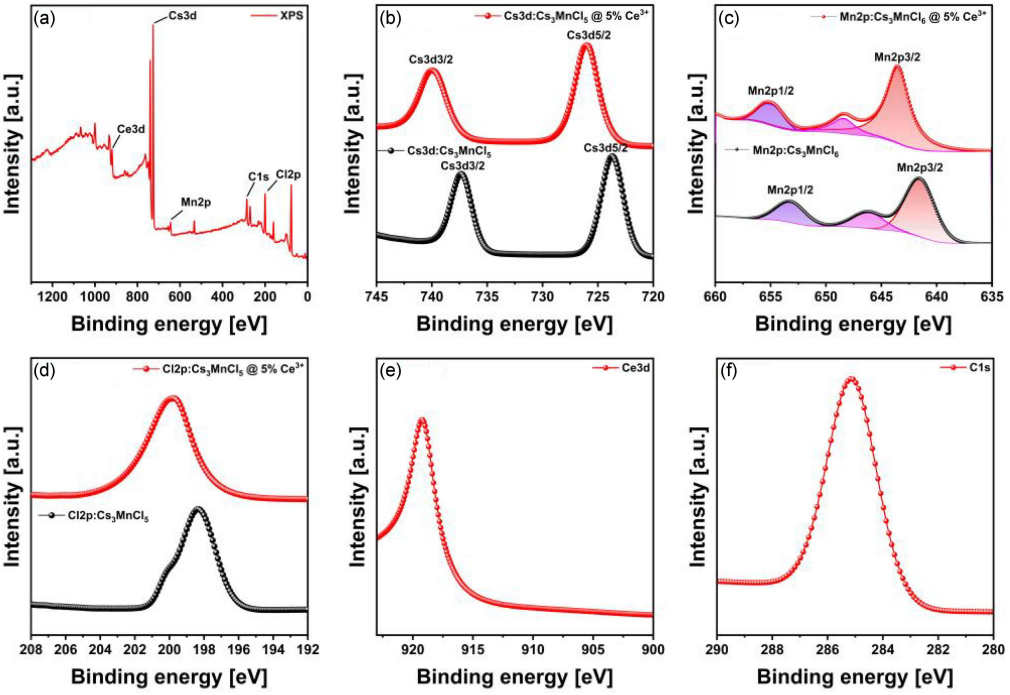

Fig. 4. XPS spectra of pristine Cs_3MnCl_5 (black lines) and 5% Ce^{3+}-doped Cs_3MnCl_5 (red lines); (a) full survey spectrum; (b) high-resolution Cs 3*d* spectra; (c) high-resolution Mn 2*p* spectra; (d) high-resolution Cl 2*p* spectra; (e) high-resolution Ce 3*d* spectrum; (f) C 1*s* reference spectrum for binding energy calibration.

and Sb^{3+} ions have been successfully incorporated into the Cs_3MnCl_5 crystal lattice by substituting Mn^{2+} ions.

To further confirm the successful incorporation of B-site dopants and investigate their influence on the local electronic environment of the host lattice,

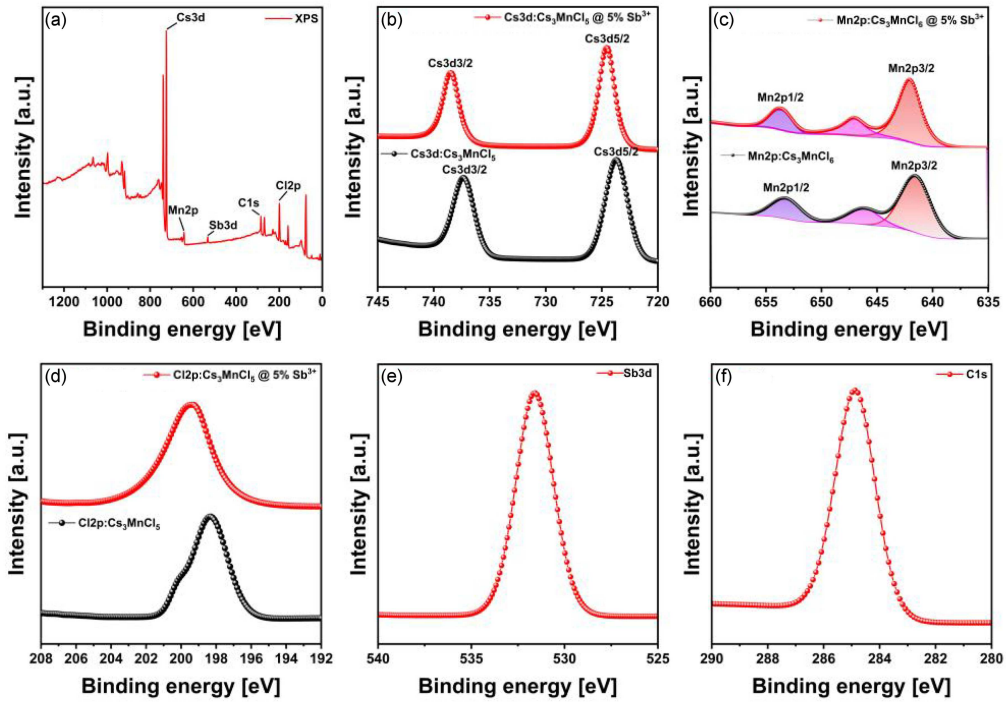

Fig. 5. XPS spectra of pristine Cs_3MnCl_5 (black lines) and 5% Sb^{3+}-doped Cs_3MnCl_5 (red lines); (a) full survey spectrum; (b) high-resolution Cs 3*d* spectra; (c) high-resolution Mn 2*p* spectra; (d) high-resolution Cl 2*p* spectra; (e) high-resolution Sb 3*d* spectrum; (f) C 1*s* reference spectrum for binding energy calibration.

XPS measurements were carried out to characterize the elemental composition, valence states, and core-level binding energy shifts of all samples. All binding energies were calibrated using the C 1*s* reference peak at 284.80 eV. The pristine Cs_3MnCl_5 sample (black curves in Figs. 3–5) was used as the reference sample for peak shift comparison, exhibiting characteristic peaks at 724.10 eV (Cs $3d_{5/2}$), 737.81 eV (Cs $3d_{3/2}$), 641.68 eV (Mn $2p_{3/2}$), 653.21 eV (Mn $2p_{1/2}$), 198.15 eV (Cl $2p_{3/2}$), and 200.09 eV (Cl $2p_{1/2}$). XPS survey spectra confirm the presence of characteristic Cs 3*d*, Mn 2*p*, and Cl 2*p* signals in all B-doped Cs_3MnCl_5 samples (B = Ag^+, Ce^{3+}, Sb^{3+}), along with faint but detectable signals corresponding to Ag 3*d* (Fig. 3a), Ce 3*d* (Fig. 4a), and Sb 3*d* (Fig. 5a), respectively. High-resolution XPS analysis consistently reveals that Mn ions remain in the +2 oxidation state in all doped samples, as evidenced by the distinct satellite peaks between the Mn $2p_{3/2}$ and Mn $2p_{1/2}$ peaks, while Cs ions maintain their monovalent oxidation state throughout the doping process. Notably, the core-level binding energies of Cs 3*d*, Mn 2*p*, and Cl 2*p* all exhibit positive shifts relative to the pristine sample, with a clear magnitude trend, namely Ce^{3+} doping induces the largest shift, while Ag^+ and Sb^{3+} doping result in similar small shifts. Specifically, the Cs $3d_{5/2}$ peaks shift by ~ 0.56 eV (Ag^+), ~ 1.86 eV (Ce^{3+}), and ~ 0.44 eV (Sb^{3+}); the Mn $2p_{3/2}$ peaks shift by ~ 0.32 eV (Ag^+), ~ 1.83 eV (Ce^{3+}), and ~ 0.37 eV (Sb^{3+}); and the Cl $2p_{3/2}$ peaks shift by ~ 0.53 eV (Ag^+), ~ 1.57 eV (Ce^{3+}), and ~ -0.09 eV (Sb^{3+}). This difference in binding energy shift magnitude can be attributed to the combined effects of dopant electronegativity, ionic radius, and oxidation state. On one hand, all dopant ions possess higher electronegativity than Mn^{2+} ($Sb^{3+} > Ag^+ > Ce^{3+} > Mn^{2+}$), which withdraws electron density from adjacent host ions and increases the core-level binding energy. On the other hand, larger dopant ionic radii cause more significant lattice distortion, which changes the overlap of electron clouds between adjacent atoms and further modulates the binding energy. Ce^{3+} shows the largest shift due to its +3 oxidation state (higher than Mn^{2+}) and relatively large ionic radius, which together exert the strongest perturbation on the local electronic environment. In contrast, the smaller shift of Ag^+ is partially offset by the charge compensation effect introduced by its +1 oxidation state, while Sb^{3+} exhibits minimal lattice distortion as its ionic radius is closest to that of Mn^{2+} [43].

In summary, these systematic binding energy changes, combined with the consistent lattice expansion trends observed in XRD, provide strong evidence for the successful substitution of B-site Mn^{2+} by Ag^+, Ce^{3+}, and Sb^{3+} ions in the Cs_3MnCl_5 lattice.

As shown in the fluorescence spectrum in Fig. 6a, at the optimal excitation wavelength of 365 nm, the sample exhibits broad-spectrum green emission at 520 nm, with corresponding CIE color space

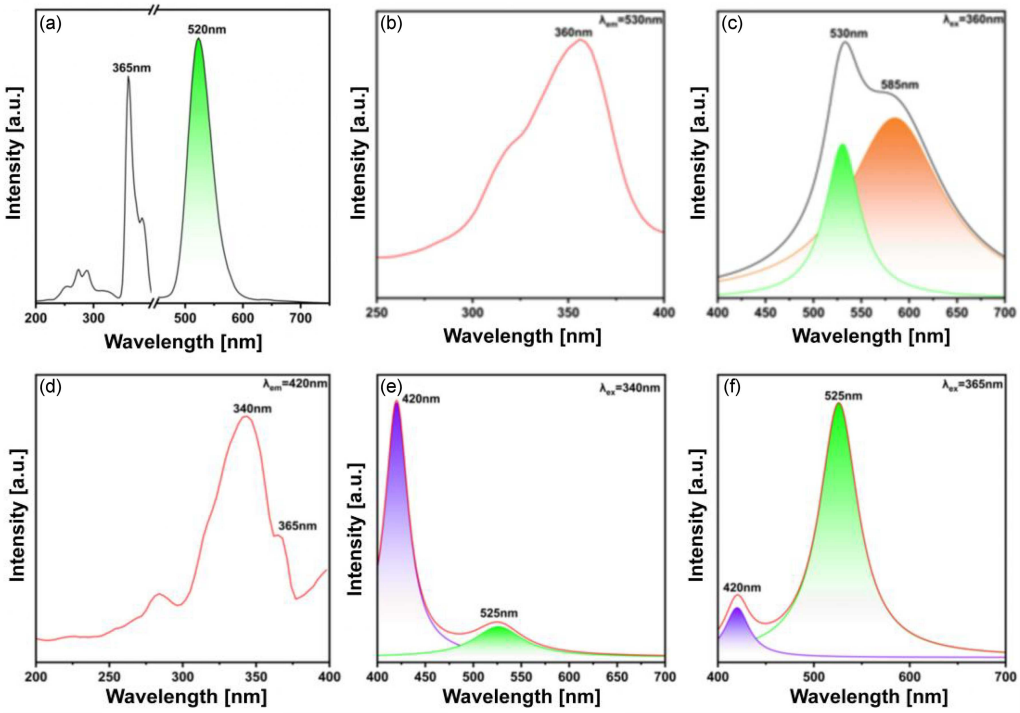

Fig. 6. Optical characterization of B-doped Cs_3MnCl_5; (a) PL and PLE of Cs_3MnCl_5; (b) PLE of Sb^{3+}-doped Cs_3MnCl_5; (c) PL of Sb^{3+}-doped Cs_3MnCl_5; (d) PLE of Ce^{3+}-doped Cs_3MnCl_5; (e) PL of Ce^{3+}-doped Cs_3MnCl_5 at 340 nm excitation; (f) PL of Ce^{3+}-doped Cs_3MnCl_5 at 365 nm excitation.

coordinates (0.2603, 0.6948) (see Fig. 7a, d). This is attributed to the fact that the luminescence of Mn^{2+} depends on the ligand field around it, typically emitting green light in a four-coordination state and orange-red light in an eight-coordination state. The optical properties are consistent with those of the Cs_3MnCl_5 single crystal prepared by the previously reported liquid-phase method [40]. Therefore, it can be determined by XRD and optical characterization that Cs_3MnCl_5 single crystals can be successfully prepared by the vacuum solid-state method, and the obtained luminescence properties are better than those of liquid-phase method. Intrinsic Cs_3MnCl_5 exhibits a 520 nm green emission originating from the $^4T_1$–$^6A_1$ transition of tetrahedrally coordinated Mn^{2+}, which is consistent with the result of XPS, as shown in Figs. 3–5. The bright green fluorescence of Cs_3MnCl_5 single crystals holds great potential in the field of lighting. However, its stability in the environment is not good. It is prone to combine with moisture in the air and transform into the dark red-emitting $Cs_2MnCl_4(H_2O)_2$ phase containing crystal water, which undoubtedly affects its application in white LEDs and pure color emission. Therefore, improving its stability in the air is urgent. Doping is a powerful means to enhance the stability of materials. We selected Mg^{2+}, Ag^+, Ga^{3+}, In^{3+}, and In^+ as the elements for B-site doping. The first reason is that they cover the cases of low-valent, high-valent, and isovalent elements. The second reason is that they are common elements used to alter properties in 0D metal halides, which may greatly enhance material stability.

In a high-humidity environment, the green fluorescence of the original Cs_3MnCl_5 single crystal begins to decrease after just 15 min. Among the other doped samples, the most stable is Ag^+-doped Cs_3MnCl_5, which maintains its green fluorescence for 36 h in a high-humidity environment before completely disappearing. Compared to the original sample, its stability has been improved by more than 10 times (Fig. 8a–f). Green fluorescence, as one of the three optical primary colors, plays an important role in white LEDs. To obtain white light from Cs_3MnCl_5 single crystals emitting green fluorescence, one approach is to mix it with blue and red fluorescence to achieve the three primary colors of light. The other approach is to mix it with purple fluorescence, using the purple fluorescence to simulate the mixed result of blue and red fluorescence. Therefore, if cations capable of inducing purple fluorescence emission are doped into the B site, it is possible to directly obtain white light. Ce^{3+} typically induces the emission of purple fluorescence. Introducing Ce^{3+} ions into the Cs_3MnCl_5 lattice results in the sample exhibiting dual-peak emission of purple and green, laying the foundation for adjusting white light. As shown in Fig. 6e, f, after the incorporation of Ce^{3+} into the Cs_3MnCl_5 lattice, a bright purple fluorescence emission is observed at 420nm, and a bright green fluorescence emission is observed

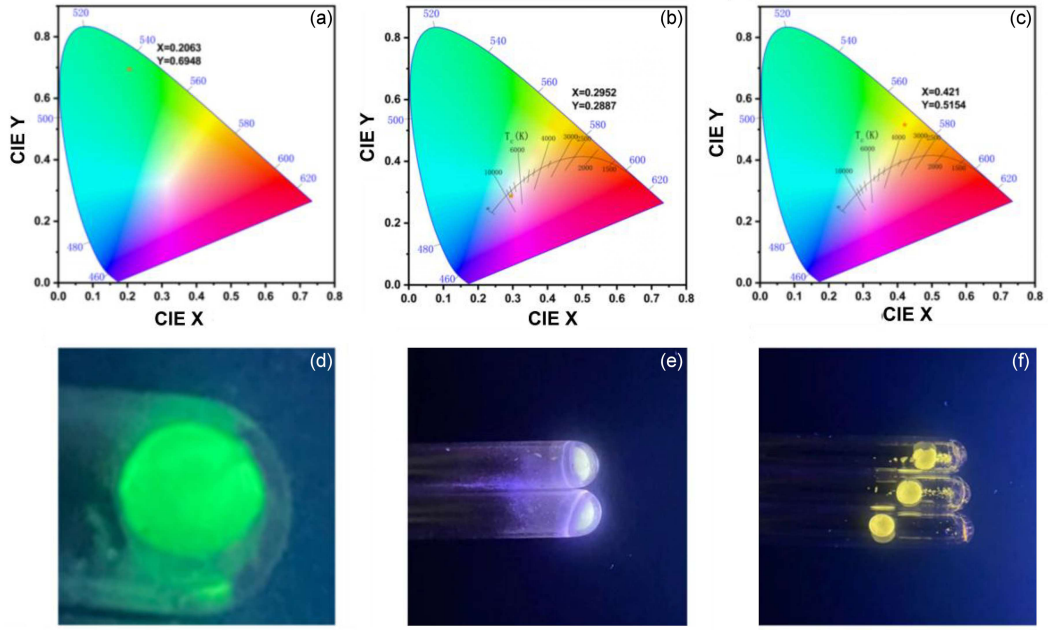

Fig. 7. Optical properties of B-doped Cs_3MnCl_5; (a) CIE coordinates of Cs_3MnCl_5; (b) CIE coordinates of Ce^{3+}-doped Cs_3MnCl_5; (c) CIE coordinates of Sb^{3+}-doped Cs_3MnCl_5; (d) physical diagram of Cs_3MnCl_5 at 365 nm excitation; (e) physical diagram of Ce^{3+}-doped Cs_3MnCl_5 at 365 nm excitation; (f) physical diagram of Sb^{3+}-doped Cs_3MnCl_5 at 365 nm excitation.

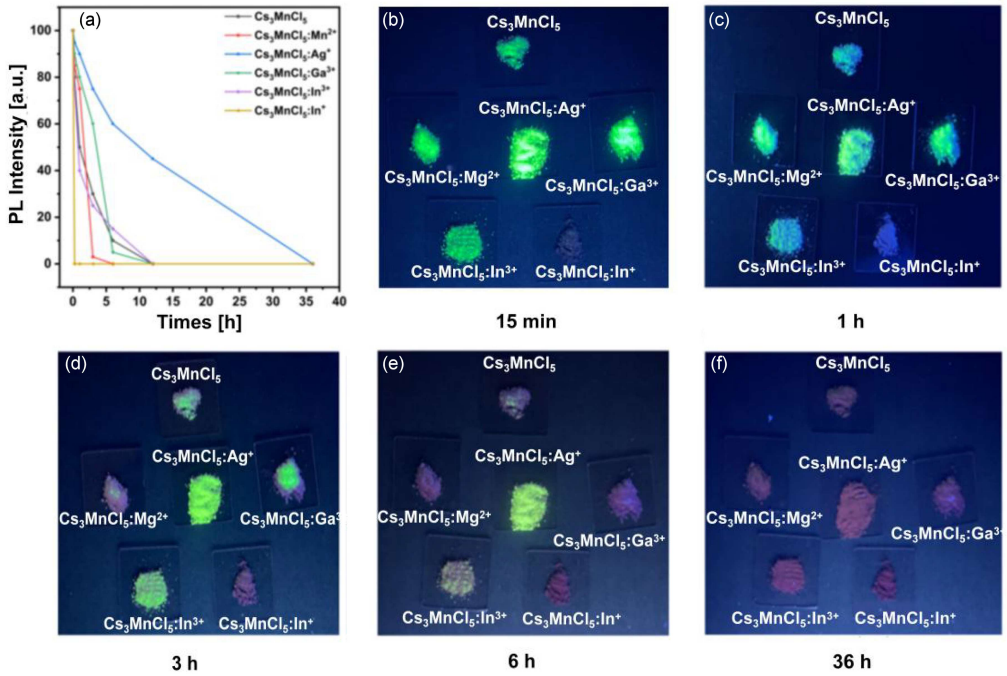

Fig. 8. Stability test of B-doped Cs_3MnCl_5; (a) PL intensity decay curve of B-doped Cs_3MnCl_5 over time (B = Ag^+, Mg^{2+}, Ga^{3+}, In^{3+}, In^+); (b–f) physical image of the decay of PL intensity of B-doped Cs_3MnCl_5 with time at 365 nm excitation.

at 520 nm. Meanwhile, according to the photoluminescence excitation (PLE) spectrum (Fig. 6d), it is found that compared to the original PLE spectrum of Cs_3MnCl_5 (Fig. 6a), the optimal excitation peak at 365 nm is significantly reduced, and instead, an additional strongest excitation peak at 340 nm appears. The excitation peak of 340 nm is derived from the d–f transition emission caused by Ce^{3+} incorporation, and the excitation peak of 365 nm is the d–d transition emission caused by Mn^{2+} inherent

in the material. The increase in the excitation peak at 340 nm and the decrease in the excitation peak at 365 nm indicate that after the sample is excited by ultraviolet light, energy is effectively transferred from the host to Ce^{3+}. Therefore, under 340 nm excitation, the purple fluorescence peak is higher than the green fluorescence peak, while under 365 nm excitation, the opposite is true, with the green fluorescence peak being higher than the purple fluorescence peak (Fig. 6e, f). This means that the ratio of the purple to green fluorescence peaks can be controlled by adjusting the excitation wavelength, thereby achieving white light under appropriate excitation, as shown in Fig. 7e. Under the irradiation of a 365 nm ultraviolet flashlight, the sample emits cool white light, with the corresponding CIE coordinates being (0.2952, 0.2877) (see Fig. 7b). After successfully achieving dual-peak emission of cool white light by doping with Ce^{3+} ions, Sb^{3+} ions, which are commonly used to break parity-forbidden transitions and introduce additional luminescent centers, are introduced in an attempt to broaden the spectrum of Cs_3MnCl_5. Optical characterization was performed on the doped sample. As shown in Fig.7f, after the addition of Sb^{3+} ions, the sample under ultraviolet irradiation changes from its original bright green color to yellow fluorescence, and the crystallization is significantly enhanced without any crystals adhering to the quartz tube wall. According to the PL spectrum (Fig. 6c), the introduction of Sb^{3+} ions brings about a broad orange emission at 585 nm, attributed to the $^3P_1$–$^1S_0$ transition of Sb^{3+}.

The obtained fluorescence spectrum data are processed in CIE software, resulting in CIE coordinates of (0.4210, 0.5154) (see Fig. 7c), corresponding to yellow–green fluorescence dominated by yellow color (Fig. 7f). Upon comparing the PL spectra of Cs_3MnCl_5, Ce^{3+}-doped Cs_3MnCl_5, and Sb^{3+}-doped Cs_3MnCl_5, it was observed that the inherent green fluorescence undergoes a slight red shift after doping. This may be attributed to the fact that the radii of the chosen doping ions are all larger than that of Mn^{2+} ions, which leads to an increase in the distance between atoms in the crystal lattice, thereby reducing the interaction between electrons. Consequently, the energy difference between the conduction band and the valence band decreases. Therefore, upon photoexcitation, the released energy is also relatively reduced, resulting in a red shift of the inherent luminescence peak [40].

4. Conclusions

In this study, high-quality all-inorganic zero-dimensional perovskite Cs_3MnCl_5 single crystals were successfully synthesized using the vacuum solid-state reaction method. This method shows significant advantages over traditional liquid-phase methods in terms of synthesis convenience and product purity. Through the B-site doping engineering system, Ag^+, Ce^{3+}, and Sb^{3+} ions were introduced. XRD and XPS analyses confirm that all three heterovalent ions successfully enter the crystal lattice and replace some Mn^{2+} sites. Due to the larger radii of the doping ions, the crystal lattice expands. Optical performance studies reveal that intrinsic Cs_3MnCl_5 exhibits a 520 nm green emission originating from the $^4T_1$–$^6A_1$ transition of tetrahedrally coordinated Mn^{2+}. Ce^{3+} doping induces dual-peak luminescence, originating from the $5d$–$4f$ transition of Ce^{3+} and the green emission of Mn^{2+}. The intensity ratio of the dual peaks can be flexibly tuned by excitation wavelength, achieving cool white light emission under 365 nm excitation (CIE coordinates being 0.2952, 0.2877). Sb^{3+} doping introduces an orange emission at 585 nm, originating from the $^3P_1$–$^1S_0$ transition of Sb^{3+}, resulting in yellow–green fluorescence (CIE coordinates being 0.4210, 0.5154). At the same time, the observed surface chlorine enrichment contributes to defect passivation. The slight red shift of the intrinsic emission peak of Mn^{2+} after doping is attributed to the reduction in the bandgap caused by lattice expansion. Through a strategy combining solid-state synthesis and doping engineering, this study successfully achieves the synergistic regulation of the stability and luminescent color of Cs_3MnCl_5 single crystals, providing an important material basis and design idea for the application of Mn-based zero-dimensional metal halide perovskites in white light-emitting diodes and multicolor anti-counterfeiting fields.

Acknowledgments

This work was supported by the National Natural Science Foundation of China (Grant No. 11004129), the Scientific Research Starting Foundation for the Returned Overseas Chinese Scholars, the Ministry of Education of China (SRF for ROCS, SEM), and the Innovation Program of Shanghai Municipal Education Commission, China (Grant No. 11YZ197).

References

[1] R. Azmi, D.S. Utomo, B. Vishal et al., *Nature* **628**, 93 (2024).

[2] K.E. Babu, N. Murali, K.V. Babu, P.T. Shibeshi, V. Veeraiah, *Acta Phys. Pol. A* **125**, 1179 (2014).

[3] C. Chen, J. Xu, X. Wang, R.G. Palgrave, *J. Mater. Chem. A* **12**, 5055 (2024).

[4] H. Li, T. Luo, S. Zhang, Z. Sun, X. He, W. Zhang, H. Chang, *Energy Environ. Mater.* **4**, 46 (2021).

[5] M. Wuttig, C.F. Schön, M. Schumacher, J. Robertson, P. Golub, E. Bousquet, C. Gatti, J.-Y. Raty, *Adv. Funct. Mater.* **32**, 2110166 (2022).

[6] M.I. Saidaminov, J. Almutlaq, S. Sarmah, I. Dursun, A.A. Zhumekenov, R. Begum, J. Pan, N. Cho, O.F. Mohammed, O.M. Bakr, *ACS Energy Lett.* **1**, 840 (2016).

[7] J. Yin, P. Maity, M. De Bastiani, I. Dursun, O.M. Bakr, J.-L. Brédas, O.F. Mohammed, *Sci. Adv.* **3**, e1701793 (2017).

[8] Q. Chen, C. Wang, K. Wang, Y. Su, G. Dong, H. Yan, *J. Mater. Chem. A* **14**, 14751 (2026).

[9] J. Nie, X. Yun, F. Cheng, B. Lan, R. Cao, J. Wang, *J. Mater. Chem. C* **12**, 2571 (2024).

[10] N. Zheng, S. Cao, T. Zhang et al., *Nat. Chem.* **17**, 1401 (2025).

[11] Y. Qi, S. Han, Y. Cao, S. Qiu, Y. Song, C. Wang, L. Cai, *Opt. Lett.* **50**, 1029 (2025).

[12] Y. Mao, J. Zhang, Q. Ren, M.S. Molokeev, G. Zhou, X.-M. Zhang, *J. Mater. Chem. C* **10**, 17638 (2022).

[13] D.-Y. Li, Y.-M. Sun, X.-Y. Wang, N.-N. Wang, X.-Y. Zhang, C.-Y. Yue, X.-W. Lei, *J. Chem. Lett.* **13**, 6635 (2022).

[14] Y. Zhang, M.I. Saidaminov, I. Dursun, H. Yang, B. Murali, E, Alarousu, E. Yengel, B.A. Alshankiti, O.M. Bakr, O.F. Mohammed, *J. Phys. Chem. Lett.* **8**, 961 (2017).

[15] T. Jun, K. Sim, S. Iimura, M. Sasase, H. Kamioka, J. Kim, H. Hosono, *Adv. Mater.* **30**, 1804547 (2018).

[16] J. Yao, C. Cao, H. Cheng, D. Wang, W. Yang, R. Xie, *J. Phys. Chem. C* **127**, 3602 (2023).

[17] M. Aftabuzzaman, T. Bhoyar, S. Jeong, S.J. Lee, R. Levan, D.H. Choi, K. Lee, *ACS Energy Lett.* **10**, 4439 (2025).

[18] U. Petralanda, G. Biffi, S.C. Boehme, D. Baranov, R. Krahne, L. Manna, I. Infante, *Nano Lett.* **21**, 8619 (2021).

[19] W.L. Xu, S.J. Bradley, Y. Xu, F. Zheng, C.R. Hall, K.P. Ghiggino, T.A. Smith, *RSC Adv.* **10**, 43579 (2020).

[20] R. Chiara, Y.O. Ciftci, V.I.E. Queloz, M.K. Nazeeruddin, G. Grancini, L. Malavasi, *J. Phys. Chem. Lett.* **11**, 618 (2020).

[21] Q. Zhang, S. Liu, M. He, et al., *Angew. Chem. Int. Ed.* **61**, e202205463 (2022).

[22] W. Nan, L. Zhang, S. Li, P. Jin, B. Zhou, Z. Yin, T. Wang, N. Ye, Z. Hu, Y. Wu, *Inorg. Chem.* **63**, 23691 (2024).

[23] H. Sakuta, S. Seo, S. Kimura, M. Hörning, K. Sadakane, T. Kenmotsu, M. Tanaka, K. Yoshikawa, *J. Phys. Chem. Lett.* **9**, 5792 (2018).

[24] P. Gao, S. Cheng, J. Liu, J. Li, Y. Guo, T. Qin, A. Wang, *Molecules* **27**, 8259 (2022).

[25] Y.-X. Wang, Z. Cai, *Phys. Rev. B* **107**, 125203 (2023).

[26] C. Wang, Y. Li, Z. Deng, *Chem. Sci.* **16**, 15796 (2025).

[27] G. Zhou, J. Ding, X. Jiang, J. Zhang, M.S. Molokeev, Q. Ren, J. Zhou, S. Lia, X.-M. Zhang, *J. Mater. Chem. C* **10**, 2095 (2022).

[28] S. Yan, W. Tian, H. Chen, K. Tang, T. Lin, G. Zhong, L. Qiu, X. Pan, W. Wang, *Adv. Funct. Mater.* **31**, 2100855 (2021).

[29] V. Morad, I. Cherniukh, L. Pöttschacher, Y. Shynkarenko, S. Yakunin, M.V. Kovalenko, *Chem. Mater.* **31**, 10161 (2019).

[30] C. Sun, H. Lu, C.Y. Yue, H. Fei, S. Wu, S. Wang, X.-W. Lei, *ACS Appl. Mater. Interfaces* **14**, 56176 (2022).

[31] J. Lin, Z. Guo, N. Sun, K. Liu, S. He, X. Chen, J. Zhao, Q. Liu, W. Yuan, *Inorg. Chem.* **61**, 15266 (2022).

[32] X. Cheng, R. Li, W. Zheng, D. Tu, X. Shang, Z. Gong, J. Xu, S. Han, X. Chen, *Adv. Opt. Mater.* **9**, 2100434 (2021).

[33] X. Liu, W. Zhang, R. Xu, J. Tu, G. Fang, Y. Pan, *Dalton Trans.* **51**, 10029 (2022).

[34] Q. Huang, T. Huang, B. Ke, Z. Yang J. Fu, M. Liu, B. Zou, *J. Phys. Chem. Lett.* **16**, 10603 (2025).

[35] H. Li, L. Tian, Q. Yang, N. Wang, X. Fu, L. Zhou, J. Feng, H. Zhang, *Sci. China Chem.* **68**, 2459 (2025).

[36] Ö. Yildiz, A.M. Soydan, A. Ata, E.F. İpçzade, D. Akin, Ö. Uçakb, *Acta Phys. Pol. A* **125**, 669 (2014).

[37] H. Xiao, P. Dang, X. Yun, G. Li, Y. Wei, Y. Wei, X. Xiao, Y. Zhao, M.S. Molokeev, Z. Cheng, J. Lin, *Angew. Chem. Int. Ed.* **60**, 3699 (2021).

[38] M. Yang, S. Cheng, F. Yang, H. Ye, Y. Chen, W. Xiang, S. Pan, X. Liang, *J. Lumin.* **253**, 119470 (2023).

[39] P. Liu, Y. Sun, A.J. Fernández-Carrión, B. Zhang, H. Fu, L. He, X. Ming, C. Yin, X. Kuang, *Chinese Chem. Lett.* **35**, 108641 (2024).

[40] J. Wang, Y. Xin, X. Xiao, N. Abbas, E. Kang, R. Jia, Y. Han, J. Tang, Z. Zhang, *Chem. Mater.* **37**, 7962 (2025).

[41] L. Li, L. Mao, J. Yang, *Adv. Mater. Technol.* **10**, 2401175 (2024).

[42] D. Moro, G. Ulian, G. Valdrč, *J. Compos. Sci.* **5**, 214 (2021).

[43] J. Bin, H. Gee, T. Park, U.J. Go, J.H. Kim, Y.-S. Lee, *Curr. Appl. Phys.* **59**, 85 (2024).